nature physics

Article

https://doi.org/10.1038/s41567-023-02380-1

Bragg glass signatures in Pd_xErTe_3 with X-ray diffraction temperature clustering

In the format provided by the authors and unedited

SUPPLEMENTARY MATERIAL

A: SCALING ARGUMENT FOR BRAGG GLASS

The energy scaling argument by Imry and Ma considering an XY model [1], and by Fukuyama and Lee considering a disordered CDW [2], indicates that only short ranged correlations are allowed in continuous symmetry broken states below 4 dimensions, based on an assumption of a disorder potential linearly coupled to the phase. However for the CDW, the true potential is non-linear and a periodic function of phase. Nattermann [3] took this periodicity into account and showed that the modified scaling argument supports the quasi-long range order of the Bragg glass. Here we recall the scaling arguments, starting with Imry and Ma's analysis and its shortcoming, and then follow Nattermann's analysis [Ref. 3] supporting the Bragg glass order in 3D. We start with a charge density wave,

$$\rho(\vec{r},\phi) = \rho_0 \cos[\vec{q}_c \cdot \vec{r} + \phi(\vec{r})] \tag{1}$$

with an incommensurate wave vector $\vec{q}_c$, a constant amplitude ρ_0 and a phase $\phi(\vec{r})$ that can spatially vary due to thermal fluctuations and disorder interactions. The interaction with quenched disorder in D spatial dimensions can be described with an elastic model whose Hamiltonian is given by [4],

$$H = \frac{C}{2}\int d^D r\ |\vec{\nabla}\phi(\vec{r})|^2 + V_0 \int d^D r\ \Sigma(\vec{r})\rho(\vec{r},\phi) \tag{2}$$

where the first term is the elastic part with C as the elastic stiffness, and the second term is the disorder potential due to quenched impurities exerting a potential V_0 on the charge density, and distributed with a probability density $\Sigma(\vec{r})$. We assume there are no topological defects in the system so that $\phi(\vec{r})$ is single valued and the elastic model is well defined, which is a necessary condition for a Bragg glass [5–7]. A spatially modulated phase $\phi(\vec{r})$ increases the elastic energy, but can lower the potential energy by conforming $\rho(\vec{r})$ to the impurity distribution. The disordered phases arise from this competition between the elastic energy cost and the potential energy gain. These phases are distinguished by the fluctuations in $\phi(\vec{r})$ relative to an arbitrary reference point $\phi(\vec{r}=0)$, given by

$$W^2(|\vec{r}|) \ = \ \overline{\langle(\phi(\vec{r}) - \phi(0))^2\rangle} \tag{3}$$

where $\langle \dots \rangle$ denotes a thermal average and $\overline{(\dots)}$ denotes a disorder ensemble average. To simplify, we fix $\phi(0) = 0$, and assume that fluctuations are spherically symmetric with respect to $\vec{r} = 0$.

We first identify the scaling of elastic energy cost from Eq. (2). For a phase that varies by an amount $W(R)$ over a distance R, the elastic energy (EE) in the volume R^D scales as

$$\text{EE} \propto \frac{1}{2} C \left(\frac{W(R)}{R}\right)^2 R^D \tag{4}$$

This shows that for $D > 2$, the elastic energy cost increases with phase fluctuations over larger distances. In the absence of disorder, this energy cost protects the long range order.

Now we discuss the scaling of the potential energy in a volume R^D. We imagine each site is independently occupied by an impurity with probability n_I, the impurity concentration. The volume includes $n_I R^D$ impurities, and each random impurity site $\vec{r}_i$ contributes a potential energy $V(\vec{r}_i)$ given by,

$$V(\vec{r}_i) = V_0\rho_0 \cos[\vec{q}_c.\vec{r}_i + \phi(\vec{r}_i)] \tag{5}$$

Imry-Ma scaling: Imry and Ma's argument is valid when $\phi(\vec{r}_i)$ is small and a linear approximation applies to Eq. (5), given by

$$V(\vec{r}_i) = V_0\rho_0 \left(\cos(\vec{q}_c \cdot \vec{r}_i) - \sin(\vec{q}_c \cdot \vec{r}_i)\phi(\vec{r}_i)\right) + \mathcal{O}(\phi^2(\vec{r}_i)) \tag{6}$$

where we can discard the first term that sets a constant offset, and the second term gives the potential energy gain from $\phi(\vec{r}_i)$. To estimate the magnitude of this energy gain in a volume R^D, we note that a typical impurity site has a position $|\vec{r}_i| \sim R$ and the phase $|\phi(\vec{r}_i)| \approx \left(\overline{\langle\phi^2(\vec{r}_i)\rangle}\right)^{1/2} \sim W(R)$. Hence, the magnitude of potential energy gain from each impurity, $V_0\rho_0\,|\sin(\vec{q}_c \cdot \vec{r}_i)\phi(\vec{r}_i)|$, has a typical value $\sim V_0\rho_0 W(R)$, and the magnitude of total potential energy (PE) scales as

$$\text{PE} \ \sim \ \left(\sqrt{n_I R^D}\right) V_0\rho_0 W(R) \tag{7}$$

where the factor $\sqrt{n_I R^D}$ follows from central limit theorem giving the root mean squared value from $n_I R^D$ independent random impurities.

Equating the elastic energy cost [Eq. (4)] to potential energy gain [Eq. (7)] gives the optimal $W(R)$ given by

$$CR^{D-2}W^2(R) \sim \left(\sqrt{n_I R^D}\right) V_0\rho_0 W(R) \tag{8}$$

$$\Rightarrow W(R) \sim \left(\frac{V_0\rho_0 n_I^{1/2}}{C}\right) R^{(4-D)/2} \tag{9}$$

For $D < 4$, $W(R)$ grows algebraically with R, tempting one to conclude that the system is short-range-ordered for arbitrarily small disorder strength. A length scale for the short range order was estimated as the length R_0 at which $W(R_0) \sim \pi$, the maximum value for the fluctuation. From Eq. (9), an estimate for this length scale R_0 (also known as the Fukuyama-Lee length [2]) is given by

$$R_0 = \left(\frac{C}{V_0\rho_0 n_I^{1/2}}\right)^{2/(4-D)} \tag{10}$$

R_0 is also a length scale that highlights the breakdown of the above scaling argument. At these length scales, $\phi(\vec{r})$ is large and inconsistent with the linear approximation in Eq. (6). The full periodic nature of the potential needs to be considered to understand the fluctuations beyond R_0.

Nattermann's scaling: Retaining the periodic nature of the potential energy in Eq. (5), we can now get the new scaling estimate for the magnitude of potential energy in a volume R^D as follows. Each impurity contributes to the potential energy by a magnitude $V_0\rho_0 \left|\cos(\vec{q}_c.\vec{r}_i + \phi(\vec{r}_i))\right| \sim V_0\rho_0 e^{-\overline{\langle\phi^2(\vec{r}_i)\rangle}/2}$. In a volume R^D, since the typical position $|\vec{r}_i| \sim R$, $V_0\rho_0 e^{-\overline{\langle\phi^2(\vec{r}_i)\rangle}/2} \sim V_0\rho_0 e^{-W^2(R)/2}$, and the total potential energy (PE) thus scales as

$$\text{PE} \sim \left(\sqrt{n_I R^D}\right) V_0\rho_0 e^{-W^2(R)/2} \tag{11}$$

where the factor $\sqrt{n_I R^D}$ follows from fluctuations of $n_I R^D$ independent random impurities.

Equating the elastic energy cost [Eq. (4)] to potential energy gain [Eq. (11)] gives the optimal $W(R)$ given by

$$CR^{D-2}W^2(R) \sim \left(\sqrt{n_I R^D}\right) V_0\rho_0 e^{-W^2(R)/2} \tag{12}$$

$$\Rightarrow W^2(R) \sim (4-D)\log(R/R_0) + \mathcal{O}\left(\log(\log(R/R_0))\right) \tag{13}$$

where R_0 is the same length scale from Eq. (10). Thus for $D < 4$, $W^2(R > R_0)$ grows logarithmically to leading order. This is the Bragg glass order.

B: SAMPLE PREPARATION AND X-RAY DETAILS

Samples were grown using a Te self-flux method as described in Ref. 8. Small amounts of Pd were included in the melt to produce the palladium intercalated crystals. Crystals produced had an area of 1-2mm across and varied in thickness with intercalation level. Since the CDW transition temperature is well characterized for different intercalation levels, resistivity measurements of the sample batches used were taken to determine the intercalation levels of the samples studied [9]. Samples were shipped to Argonne in sealed vials filled with inert gas and removed and mounted on the tips of polyimide capillaries just before measurement to avoid degradation from water and oxygen exposure. During measurements, samples were cooled using an Oxford N-Helix Cryostream, which surrounded samples with either N_2 or He gas. Measurements were taken with incident x-ray energy of 87 keV in transmission geometry, with samples continuously rotated at 1° s^{-1} and a Pilatus 2M CdTe detector taking images at 10 Hz. For each sample at each temperature, three such 365° rotation scans were collected, with the detector slightly offset and the rotation angle slightly changed to fill in detector gaps and allow for removal of detector artifacts (detailed in Ref. 10).

C: PEAK WIDTH OF A DISORDERED CDW

We describe the relationship between the CDW peak width and the density correlations in a Bragg glass and short-range-ordered phase, following the analysis from Refs. [4, 11, 12]. Consider a 3D lattice with N sites, and atoms

arranged at $\vec{r}_n = \vec{R}_n + \vec{c}_n$ where $\vec{R}_n$ are the crystal lattice positions, and $\vec{c}_n$ are the lattice displacements due to a CDW. Let us describe the lattice displacements due to a unidirectional CDW with an incommensurate modulation vector $\vec{q}_c$, given by

$$\vec{c}_n = \vec{c}_0 \cos(\vec{q}_c \cdot \vec{R}_n + \phi_n) \tag{14}$$

where ϕ_n is a non uniform phase with fluctuations due to disorder interaction, and $\vec{c}_0$ is a uniform amplitude (amplitude fluctuations are energetically more expensive, hence neglected). The scattering intensity at a momentum $\vec{Q}$ is given by

$$I(\vec{Q}) \;=\; \sum_{n,m} e^{i\vec{Q}\cdot(\vec{R}_n - \vec{R}_m)} \langle e^{i\vec{Q}\cdot(\vec{c}_n - \vec{c}_m)} \rangle_\phi \tag{15}$$

where $\langle \cdots \rangle_\phi$ denotes ensemble average over disordered phase configurations $\{\phi_n\}$, and we assume a uniform disorder averaged form factor set to unity for all atoms. For small $\vec{c}_0$, the $I(\vec{Q})$ is simplified to,

$$\begin{aligned} I(\vec{Q}) \;&=\; \sum_{n,m} e^{i\vec{Q}\cdot(\vec{R}_n - \vec{R}_m)} \left[1 - \frac{1}{2} \langle \Big(\vec{Q} \cdot (\vec{c}_n - \vec{c}_m) \Big)^2 \rangle_\phi \right] + \mathcal{O}(|\vec{Q} \cdot \vec{c}_0|^4) \\ &\approx\; \sum_{n,m} e^{i\vec{Q}\cdot(\vec{R}_n - \vec{R}_m)} \left[\left(1 - \frac{1}{2} (\vec{Q} \cdot \vec{c}_0)^2 \right) + \frac{1}{4} (\vec{Q} \cdot \vec{c}_0)^2 \left(e^{i\vec{q}_c \cdot (\vec{R}_n - \vec{R}_m)} \langle e^{i(\phi_n - \phi_m)} \rangle_\phi + e^{-i\vec{q}_c \cdot (\vec{R}_n - \vec{R}_m)} \langle e^{-i(\phi_n - \phi_m)} \rangle_\phi \right) \right] \end{aligned}$$

From the above expression, we can deduce the two CDW satellite peaks at $\vec{Q} = \vec{G} \pm \vec{q}_c$ around each Bragg peak at $\vec{G}$. Focusing on the satellite peak around $\vec{G} + \vec{q}_c$, the intensity profile is given by

$$I(\vec{Q} = \vec{G} + \vec{q}_c + \delta\vec{q}) \;=\; \frac{1}{4} (\vec{Q} \cdot \vec{c}_0)^2 \sum_{n,m} e^{i\delta\vec{q}\cdot(\vec{R}_n - \vec{R}_m)} \langle e^{-i(\phi_n - \phi_m)} \rangle_\phi \tag{16}$$

where $|\delta\vec{q}| \ll |\vec{q}_c|$. The density correlations $\langle e^{-i(\phi_n - \phi_m)} \rangle_\phi$, which using the Gaussian approximation for small fluctuations get simplified to,

$$\langle e^{-i(\phi_n - \phi_m)} \rangle_\phi \;=\; e^{-\frac{1}{2}\langle (\phi_n - \phi_m)^2 \rangle_\phi} + \mathcal{O}[\langle (\phi_n - \phi_m)^4 \rangle_\phi]. \tag{17}$$

Due to translational symmetry of the disorder averaged phase fluctuations, we can define the density correlation function in terms of fluctuations relative to a reference point, given by

$$C_\phi(\vec{r}) = e^{-\frac{1}{2}\langle (\phi(\vec{r}) - \phi(0))^2 \rangle_\phi}, \tag{18}$$

where $\phi(\vec{r} = \vec{R}_n) \equiv \phi_n$. Substituting Eq. (17) and (18) in Eq. (16), we get the CDW satellite intensity as

$$I(\vec{Q} = \vec{G} + \vec{q}_c + \delta\vec{q}) \approx \frac{1}{4} (\vec{Q} \cdot \vec{c}_0)^2 N v^{-1} \int (d^3\vec{r}) e^{i\delta\vec{q}\cdot\vec{r}} C_\phi(\vec{r}) \tag{19}$$

where we have replaced the discrete lattice sum with an integral over $\vec{r} \equiv \vec{R}_n - \vec{R}_m$, and v^{-1} is the volume of a unit cell. The profile of the CDW peak is thus determined by $C_\phi(\vec{r})$, whose long distance behavior distinguishes long-range-ordered, Bragg glass, and short-range-ordered CDW phases.

1. Long range ordered CDW: $C_\phi(\vec{r} \to \infty) \neq 0$ for a CDW with perfect long range ordered phase. Here, Eq. (19) gives delta function peaks with ideally zero peak width.

2. Short range ordered CDW: When $C_\phi(\vec{r}) \sim e^{-r/\zeta}$, with a correlation length ζ, Eq. (19) gives a broadened (nearly Lorentzian) peak at $\vec{Q} = \vec{G} \pm \vec{q}_c + \delta\vec{q}$ given by

$$I(\vec{Q}) \propto (\vec{Q} \cdot \vec{c}_0)^2 \zeta^3 \frac{1}{(1 + \zeta^2 |\delta\vec{q}|^2)^2} \tag{20}$$

whose full width at half maxima (FWHM) is $(2\sqrt{\sqrt{2} - 1})\zeta^{-1}$. Thus the observed peak width is determined by the inverse phase correlation length ζ^{-1}, and is independent of the momentum $\vec{Q}$ of the peak.

3. Bragg glass ordered CDW: A Bragg glass phase is distinguished by a power law decaying phase correlation: $C_\phi(r > R_0) \sim (r/R_0)^{-\eta}$ where $\eta \approx 1$ in 3D is a universal exponent as shown by Refs. [5, 13], and R_0 is a small

distance cut-off [see Eq. 10] that sets the onset of power law decay. For the Bragg glass, Eq. (19) in the limit $|\delta\vec{q}| \to 0$ can be solved to get the intensity at $\vec{Q} = \vec{G} \pm \vec{q}_c + \delta\vec{q}$ as

$$I(\vec{Q}) \ \propto \ \left(|\delta\vec{q}|^{\eta-3}\right)(\vec{Q}\cdot\vec{c}_0)^2 R_0^{\eta} \tag{21}$$

For 3D where $\eta = 1$, the peak intensity of a Bragg glass diverges as $|\delta\vec{q}|^{-2}$. As with long range order, the observed width will be the resolution limit of the detector [4].

D: DISORDER PINNING AND ASYMMETRY

Here we show that the presence of an asymmetry between the satellite peak intensities signals the disorder pinning of lattice modulations. The derivation below follows from Refs [11, 14]. While the asymmetry signature was experimentally observed for short range ordered CDW materials [11, 15, 16], they were also predicted to occur in Bragg glass ordered CDW in Ref. [4, 12].

Consider a 3D lattice with atoms arranged at $\vec{r}_n = \vec{R}_n + \vec{u}_n$ where $\vec{R}_n$ are the crystal lattice positions and $\vec{u}_n$ is a displacement from the n^{th} lattice site. The Fourier component of the displacement modulation is given by

$$\vec{u}_{\vec{q}} = N^{-1/2}\sum_n \vec{u}_n e^{-i\vec{q}\cdot\vec{R}_n} \tag{22}$$

where N is the total number of sites. Let us model the intercalation (disorder) as modifying the original form factor to a new value f_j at random sites j. The Fourier component of the modulated form factor is given by

$$\tilde{f}_{\vec{q}} = N^{-1/2}\sum_n f_n e^{-i\vec{q}\cdot\vec{R}_n}. \tag{23}$$

The scattering intensity at a momentum $\mathcal{Q}$ for this model with intercalation disorder and small lattice displacements is given by

$$I(\vec{Q}) \ = \ \sum_{n,m} e^{i\vec{Q}\cdot(\vec{R}_n-\vec{R}_m)}\langle f_n f_m e^{i\vec{Q}\cdot(\vec{u}_n-\vec{u}_m)}\rangle \tag{24}$$

$$= \ \sum_{n,m} e^{i\vec{Q}\cdot(\vec{R}_n-\vec{R}_m)}\langle f_n f_m \left[1 + i\vec{Q}\cdot(\vec{u}_n-\vec{u}_m)\right]\rangle + \mathcal{O}\left(|\vec{Q}\cdot(\vec{u}_n-\vec{u}_m)|^2\right) \tag{25}$$

where $\langle\cdots\rangle$ denotes thermal and disorder average.

We are interested in the asymmetry of the intensities $I(\vec{Q})$ between the two satellite points $\vec{G}\pm\vec{q}$ across a Bragg peak at $\vec{G}$, where $\vec{q}$ is within the first Brillouin zone. Substituting the inverse Fourier transforms of Eq. (22) for $\vec{u}_i$ and Eq. (23) for f_i in to Eq. (25), we get the satellite asymmetry to be

$$I(\vec{G}+\vec{q}) - I(\vec{G}-\vec{q}) = 2i\tilde{f}_0\vec{G}\cdot\left(\langle\vec{u}_{-\vec{q}}\tilde{f}_{\vec{q}}\rangle - \langle\vec{u}_{\vec{q}}\tilde{f}_{-\vec{q}}\rangle\right) + \mathcal{O}\left(|\vec{G}\cdot\vec{u}_{\vec{q}}|^2\right) \tag{26}$$

where $N^{-1/2}\tilde{f}_0 = N^{-1}\sum_j f_j$ is the average form factor of the disordered lattice. If the lattice displacement modulations are not correlated with the intercalant positions (no disorder pinning), then the term $\langle\vec{u}_{\vec{q}}\tilde{f}_{-\vec{q}}\rangle = \langle\vec{u}_{\vec{q}}\rangle\langle\tilde{f}_{-\vec{q}}\rangle = 0$ since $\langle\vec{u}_{\vec{q}}\rangle = \langle\vec{u}_{-\vec{q}}\rangle = 0$. The $\langle\vec{u}_{\vec{q}}\rangle = 0$ is true for both incommensurate long range ordered CDW (since the CDW phase in each disorder configuration is arbitrary) and for short range ordered displacements (the disorder average of the displacements is zero). Thus the leading order contribution to the intensity asymmetry is zero in the absence of disorder pinning of lattice modulations.

On the other hand, in the presence of disorder pinning, $\langle\vec{u}_{\vec{q}}\tilde{f}_{-\vec{q}}\rangle \neq \langle\vec{u}_{\vec{q}}\rangle\langle\tilde{f}_{-\vec{q}}\rangle$ and hence not trivially 0. To explicitly see this non-vanishing of satellite asymmetry from disorder pinning, we discuss a simple model put forward in Ref. [15]. Consider a single impurity at a random site $\vec{R}_0$ that interacts with the charge density such that the phase of the charge density is fixed to a value ϕ_0 at site $\vec{R}_0$. The pinned CDW is given by $\rho_n = \rho_0\sin\left[\vec{q}_c\cdot(\vec{R}_n-\vec{R}_0)+\phi_0\right]$. The lattice modulations are in quadrature with the CDW and is given by $\vec{u}_n = \vec{u}_0\cos\left[\vec{q}_c\cdot(\vec{R}_n-\vec{R}_0)+\phi_0\right]$. Taking f_I as the atomic form factor of the impurity and f_0 as that of the pure atom, the satellite asymmetry [Eq. (26)] for this single impurity pinning gives,

$$I(\vec{G}+\vec{q}) - I(\vec{G}-\vec{q}) = 2N^{-1/2}f_0(f_I-f_0)(\vec{G}\cdot\vec{u}_0)\sin(\phi_0) \tag{27}$$

A maximum asymmetry is when $(f_I - f_0)\sin(\phi_0) = 1$ which corresponds to the CDW having a maximum or minimum over the impurity depending on whether the interaction is attractive or repulsive. This picture describes strong pinning, where the CDW is pinned to a constant phase ϕ_0 above each impurity. However, the pinning for a Bragg glass is weak, where the phase is modulated by the collective interaction of impurities. A calculation of the asymmetry for Bragg glass was carried out in Refs. 12 and 4, and was shown to be an experimentally observable effect in principle.

E: MOMENTUM DEPENDENCE OF CDW PEAK WIDTH

In addition to the phase fluctuations that destroy long range CDW order, displacement of atoms from their ideal lattice sites (displacement fluctuations) that destroy long range lattice order will also contribute to the broadening of the CDW peaks. Here we show that the width due to displacement fluctuations is momentum ($\vec{Q}$) dependent, in contrast to the $\vec{Q}$ independent broadening due to CDW phase fluctuations. Our model is similar to that of a paracrystal [chapter. 9 of Ref.[14]], with the modification of introducing a CDW with phase fluctuations on top of the lattice displacements. Using the same 3D lattice with N sites as in SM-B, but with an additional lattice displacement $\vec{u}_n$ that can arise from thermal vibrations or disorder interaction, the atoms are arranged at $\vec{r}_n = \vec{R}_n + \vec{c}_n + \vec{u}_n$ where $\vec{R}_n$ are the lattice sites and $\vec{c}_n$ are the CDW displacements. The scattering intensity at a momentum $\vec{Q}$ [Eq. (15)] is modified for the disordered lattice as,

$$I(\vec{Q}) \;=\; \sum_{n,m} e^{i\vec{Q}\cdot(\vec{R}_n - \vec{R}_m)} \langle e^{i\vec{Q}\cdot(\vec{c}_n - \vec{c}_m)} \rangle_\phi \langle e^{i\vec{Q}\cdot(\vec{u}_n - \vec{u}_m)} \rangle_u \tag{28}$$

where $\langle \cdots \rangle_u$ denotes ensemble average over lattice displacement configurations $\{u_n\}$, and we have assumed the lattice displacements are uncorrelated with the phase fluctuations. The CDW intensity around $\vec{Q} = \vec{G} + \vec{q}_c$ in Eq. (16) is now modified to

$$I(\vec{Q} = \vec{G} + \vec{q}_c + \delta\vec{q}) \;=\; \frac{1}{4}(\vec{Q}\cdot\vec{c}_0)^2 \sum_{n,m} e^{i\delta\vec{q}\cdot(\vec{R}_n - \vec{R}_m)} \langle e^{-i(\phi_n - \phi_m)} \rangle_\phi \langle e^{-i\vec{Q}\cdot(\vec{u}_n - \vec{u}_m)} \rangle_u \tag{29}$$

where the factor $\langle e^{-i\vec{Q}\cdot(\vec{u}_n - \vec{u}_m)} \rangle_u$ under the Gaussian approximation gives

$$\langle e^{-i\vec{Q}\cdot(\vec{u}_n - \vec{u}_m)} \rangle_u \;=\; e^{-\frac{1}{2}\langle(\vec{Q}\cdot(\vec{u}_n - \vec{u}_m))^2\rangle_u} + \mathcal{O}[\langle(\vec{Q}\cdot(\vec{u}_n - \vec{u}_m))^4\rangle_u]. \tag{30}$$

where $\langle(\vec{Q}\cdot(\vec{u}_n - \vec{u}_m))^2\rangle_u$ quantify the mean squared fluctuations in relative lattice displacements. Defining a correlation function $C_u(\vec{r}, \vec{Q})$ for the displacements relative to a reference point given by,

$$C_u(\vec{r}, \vec{Q}) = e^{-\frac{1}{2}\langle\left(\vec{Q}\cdot(\vec{u}(\vec{r}) - \vec{u}(0))\right)^2\rangle_u}, \tag{31}$$

where $\vec{u}(\vec{R}_n) \equiv \vec{u}_n$, the CDW peak intensity in Eq. (19) is modified to,

$$I(\vec{Q} = \vec{G} + \vec{q}_c + \delta\vec{q}) \approx \frac{1}{4}(\vec{Q}\cdot\vec{c}_0)^2 N v^{-1} \int (d^3\vec{r}) e^{i\delta\vec{q}\cdot\vec{r}} C_\phi(\vec{r}) C_u(\vec{r}, \vec{Q}) \tag{32}$$

What sets the displacement fluctuations apart from CDW phase fluctuations is the $\vec{Q}$ dependence of $C_u(\vec{r}, \vec{Q})$. It is this distinction that leads to the $\vec{Q}$ dependent broadening signature for the displacement fluctuations. To see this, consider an exponentially decaying form for the displacement correlation given by $C_u(\vec{r}, \vec{Q}) \sim e^{-|\vec{Q}|^2(\gamma_u r)}$. Here γ_u with dimensions of length can be interpreted as the root mean square value of the relative displacement between neighboring atoms. When combined with the short range phase correlation $C_\phi(\vec{r}) \sim e^{-r/\zeta_\phi}$, Eq. (32) gives an approximately Lorentzian peak profile at $\vec{Q} = \vec{G} \pm \vec{q}_c + \delta\vec{q}$ given by

$$I(\vec{Q}) \propto \frac{1}{\left(1 + \dfrac{|\delta\vec{q}|^2}{(\zeta_\phi^{-1} + |\vec{Q}|^2\gamma_u)^2}\right)^2} \tag{33}$$

whose full width at half maxima (FWHM) is given by

$$\text{FWHM} \;\propto\; \zeta_\phi^{-1} + |\vec{Q}|^2\gamma_u \tag{34}$$

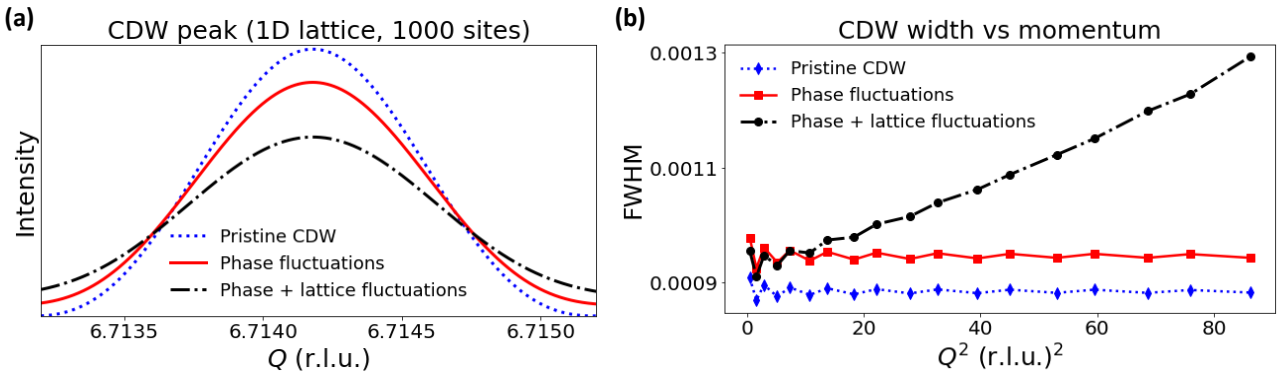

FIG. 1. **(a):** Numerically calculated intensity of a CDW peak, and **(b):** the momentum (Q) dependence of the full width at half maxima (FWHM) of the CDW peaks, in a 1D lattice with 1000 sites. The intensities are calculated for three disorder configurations: (1) pristine CDW with no disorder, (2) CDW with only phase fluctuations and (3) CDW with both phase and lattice fluctuations. Both configurations (2) and (3) lead to a broadening of the peak [panel(a)]. However, the FWHM remains independent of Q for the configuration with only phase fluctuations, while the FWHM for the configuration with both phase and lattice fluctuations show a Q^2 dependence. From the intercept of the Q^2 dependent FWHM, we can isolate the broadening contribution of the phase fluctuations.

This shows the quadratic in momentum broadening due to displacement fluctuations. While the above form was obtained for a simple displacement correlation function that decay isotropically, a more general form for the broadening would be

$$\text{FWHM} \;\propto\; \zeta_\phi^{-1} + \gamma_H Q_H^2 + \gamma_K Q_K^2 + \gamma_L Q_L^2 \tag{35}$$

and we do not include terms like $Q_H Q_K$ etc. as they violate the reflection symmetry of the lattice. From a quadratic fit to the momentum dependence of the FWHM, the contribution from phase fluctuations: ζ_ϕ^{-1} can be extracted as the intercept.

The momentum dependence of the widths were studied in the 1980's but for quasi one dimensional ordered materials with short range order [17–20]. Such an analysis in 3D materials has so far remained a challenge due to the large number of peaks in the reciprocal space that need to be analyzed.

Numerical illustration of momentum dependent peak broadening: To complement the above derivation, we numerically calculate the scattering intensity [Eq. (28)] for a 1D lattice model with short range ordered CDW phase and lattice displacements.

On a lattice with 1000 sites, we set the CDW modulation $q_c = 2/7$ to mimic the CDW of RTe_3, and set the CDW amplitude = 0.01. To generate a disordered phase configuration with short range correlation $C_\phi(|n-m|) \sim e^{-|n-m|/\zeta_\phi}$ between sites n and m, we start with the $n = 0$ site where $\phi_0 = 0$ and the phases ϕ_n for each site $n > 0$ are selected as $\phi_n = \phi_{n-1} + d\phi$ where $d\phi$ is drawn from a normal distribution with zero mean and standard deviation σ_ϕ (=0.025). This distribution generates phases whose mean square fluctuations are given by $\langle(\phi_n - \phi_m)^2\rangle_\phi = |n-m|\sigma_\phi^2$, and the phase correlation [Eq. (18)] given by $C_\phi(|n-m|) = e^{-|n-m|\sigma_\phi^2/2}$. Similarly, to generate a short ranged lattice displacement configuration, the lattice displacements u_n are generated as $u_n = u_{n-1} + du$ where du is drawn from a normal distribution with zero mean and standard deviation σ_u (=0.001), starting with $u_0 = 0$. This generates displacement configurations with mean squared fluctuation $\langle(u_n - u_m)^2\rangle_u = |n-m|\sigma_u^2$. We generate 400 realizations of phase and displacement configurations and calculate the intensity using Eq. (28).

We show the calculated intensity profile of a CDW peak and the momentum (Q) dependence of the peak width in SM Fig. 1. We see that while a short range ordered phase broadens the CDW peak whose width is independent of Q, a short range ordered lattice leads to broadening that is proportional to Q^2. In the presence of both short range ordered phase and lattice displacements, the Q independent broadening due to phase only disorder can be extracted from the intercept of the Q^2 broadening.

F: X-RAY TEMPERATURE CLUSTERING: *X-TEC*

The underlying principle of *X-TEC* is to identify the distinct temperature trajectories through a Gaussian mixture model clustering [21]. In SM-Fig. 2, we show a simplified illustration of the GMM in action. A collection of

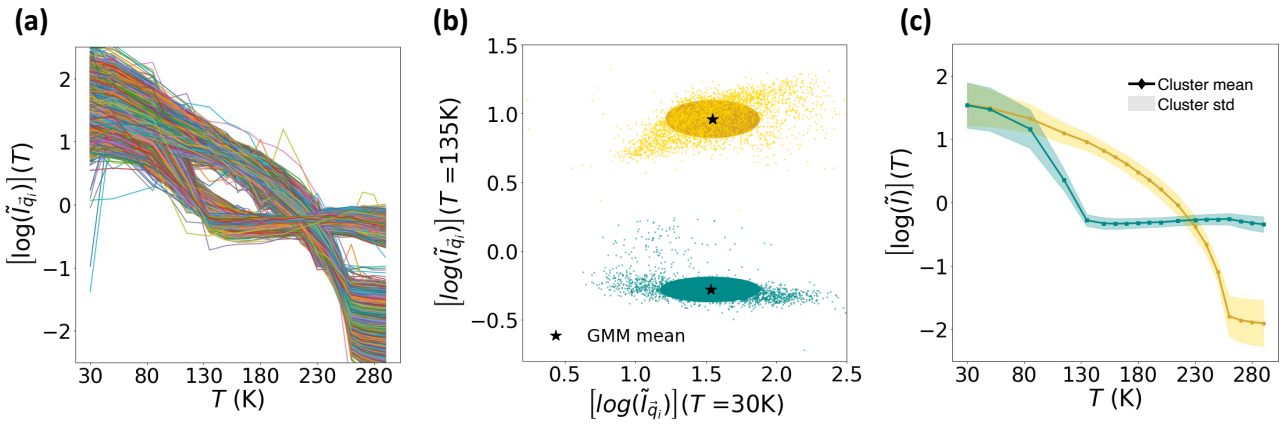

FIG. 2. A simplified illustration of *X-TEC* to cluster distinct intensity-temperature trajectories, $I(T)$, given the collection of series $\{I_{\vec{q}}(T_1), I_{\vec{q}}(T_2), \ldots, I_{\vec{q}}(T_d)\}$ ($d = 19$ in this figure) at various momentum $\vec{q}$ in the reciprocal space. The raw trajectories rescaled as $\log[\tilde{I}_{\vec{q}}(T_i)] = \log[I_{\vec{q}}(T_i)] - \langle \log[I_{\vec{q}}(T_i)] \rangle_T$ [panel (a)] can be mapped to a simple Gaussian Mixture Model (GMM) clustering problem on a d-dimensional space, whose 2D projection (along $T = 30$K and $T = 135$K) is shown in panel (b). The GMM identifies two distinct clusters and assigns them different colors. From the cluster means (star symbol) and standard deviations (colored ellipsoids) of the GMM [panel (b)], we get the distinct trajectories of $\log[\tilde{I}(T)]$ and their standard deviation, with colors reflecting their cluster assignments [panel (c)].

raw intensity-temperature trajectories [SM-Fig. 2(a)] given by $\{I_{\vec{q}}(T_1), I_{\vec{q}}(T_2), \ldots, I_{\vec{q}}(T_d)\}$ at various momenta $\vec{q}$ in reciprocal space can be represented as a distribution of points in a d dimensional hyperspace, whose axis spans the intensities at each temperature. For visualization, a 2D cross-section of this hyperspace is shown in SM-Fig. 2(b). The figure shows that the points are separated into two distinct groups (clusters). A Gaussian Mixture Model (GMM) clustering classifies these points into different clusters and assigns a mean and standard deviation for each cluster. The cluster mean reveals the distinct temperature trajectories in the data [SM-Fig. 2(c)], while the standard deviation shows that the clusters are well separated. In this example, a visual inspection of the raw intensities and a 2D projection can reveal the distinct clusters. However, the real data is messier [See Fig. 1(e)] and requires a GMM clustering on the entire hyperspace to identify the distinct trajectories.

XTEC analysis of intercalated samples

In the Fig. 2 (a-c) of the main text, we benchmarked the XTEC clustering on the pristine sample. In this section [and SM Fig. 3], we provide further details on the X-TEC analysis, using $x = 2\%$ intercalation as a representative example. We list the details in the following steps,

1. All the intensity slices in the (H, L) plane with integer K values are loaded. The first preprocessing step is the automated thresholding that removes the low-intensity background noise, as explained in Ref [21].

2. Next, we implement XTEC with label smoothing (XTEC-s) through peak averaging (Ref [21]). For this,each set of connected pixels (that passed the thresholding) in the reciprocal space is identified as a single peak. The intensity of each peak is given by its peak average value. This step removes the resolution-limited pixel-to-pixel fluctuations in the intensity. After this step, $\sim 100,000$ non-Bragg peaks are identified, which include CDWs, detector artifacts, and background scattering.

3. The peak averaged intensities are rescaled as $\overline{\log[I_{\vec{q}}(T_i)]} = \log[I_{\vec{q}}(T_i)] - \langle \log[I_{\vec{q}}(T_i)] \rangle_T$. This step ensures that the clustering reveals the distinct intensity-temperature trajectories rather than the absolute magnitude of intensities.

4. The next step is to identify the optimal number of clusters. A Bayesian information criterion (BIC) [22, 23] can provide a heuristic estimate of the optimal number. For the 2% intercalation shown in SM Fig 3(a), the elbow method roughly points to 4 or 10 clusters. To move forward, a physicist's intervention is required to identify and interpret each cluster.

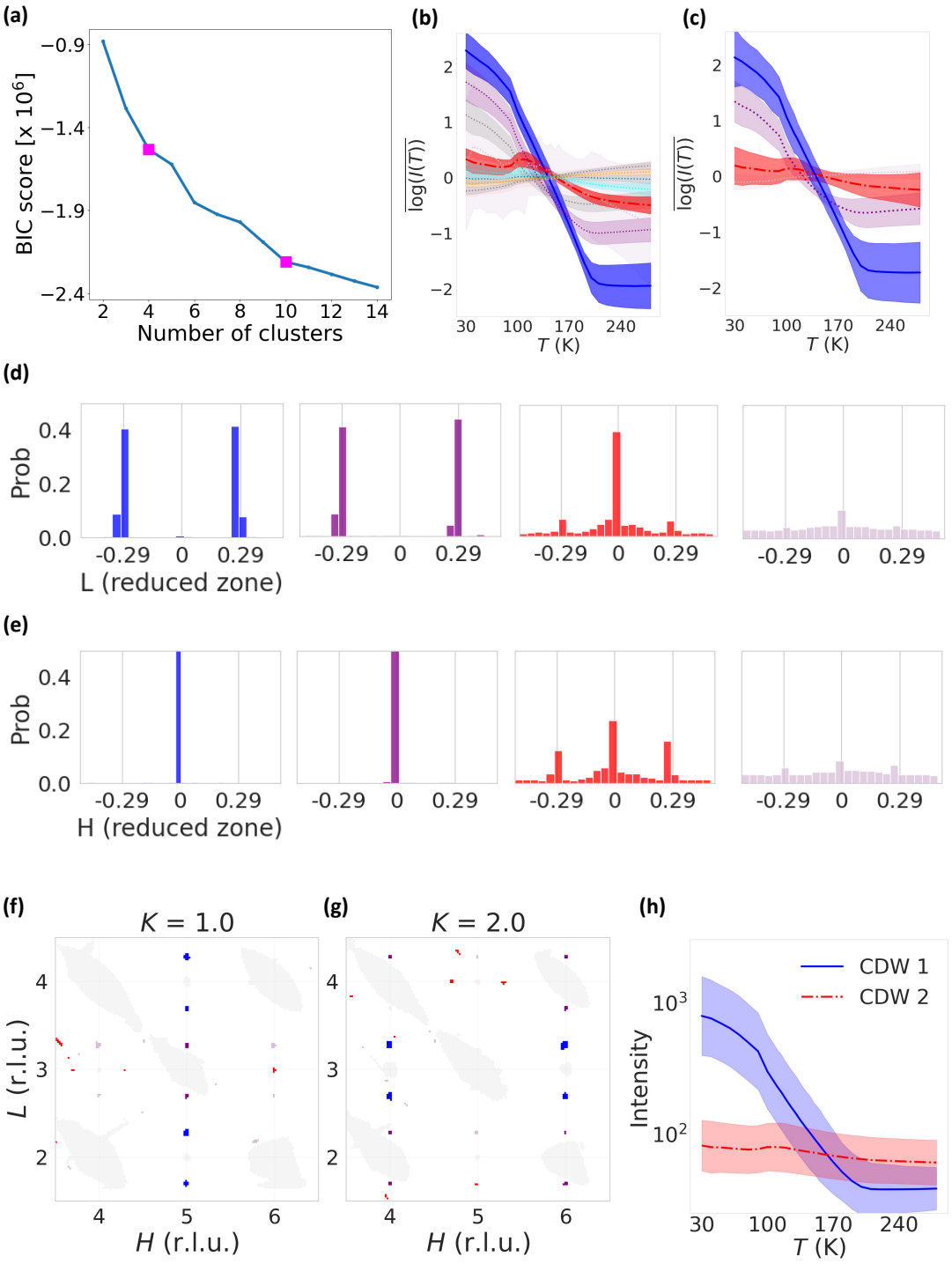

FIG. 3. Interpreting clusters for the x=2% intercalation. **(a):** The BIC score for different numbers of clusters. Two heuristic estimates of 4 and 10 clusters are marked. **(b,c):** Cluster mean (lines) and variance as one standard deviation (shaded region) for GMM with 10 clusters in (b) and 4 clusters in (c). **(d,e):** Probability distribution of the 4 clusters in (c) along L (panel (d)) and H (panel (e)) axis of the reduced Brillouin zone. **(f,g):** Distribution of the 4 clusters in the H-L plane at $K = 1$ (panel (f)) and $K = 2$ (panel (g)). **(h):** Mean (lines) and one standard deviation (shading) of the intensity-temperature trajectories in the CDW-1 (blue) and CDW-2 (red) clusters.

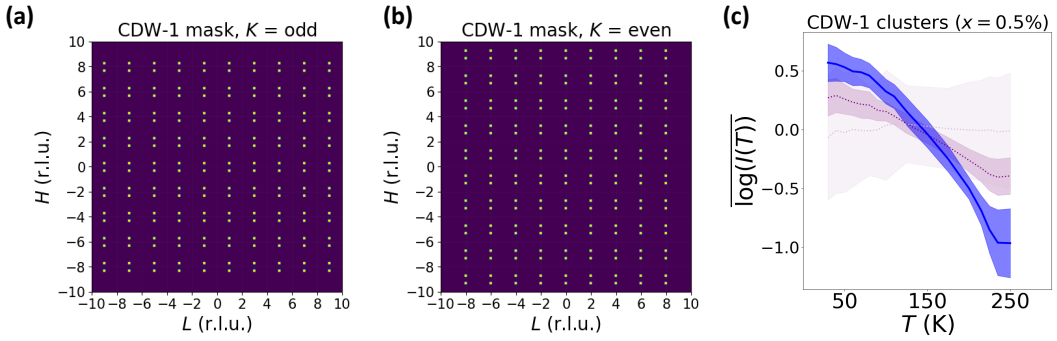

FIG. 4. CDW-1 masks for the **(a):** K = odd planes and **(b):** K = even planes. **(c):** The cluster mean (lines) and variance (shading) of the *X-TEC* clustering with three clusters of CDW-1 trajectories filtered with the mask. This eliminates the weak and noisy peaks (purple and thistle colored) to isolate the CDW-1 peaks with well-defined trajectories (blue).

SM Fig. 3 (b) and (c) show the clustered trajectories given by the cluster mean and one standard deviation of each cluster. From the trajectories, we see that 4 clusters are sufficient to reveal all the unique trajectories. To understand the physical significance of each cluster, we analyze the location of each cluster in the momentum space. For the 2% intercalation, as shown in SM Fig. 3 (d,e), we see that the blue and purple cluster is predominantly made of pixels located at $(H, L) \equiv (0, 0.29)$ corresponding to CDW-1, while the red clusters are located at $(H, L) \equiv (0.29, 0)$ corresponding to CDW-2. The last cluster (thistle colored) has no characteristic location in the momentum space and corresponds to the background intensity. The reciprocal space with the pixels assigned their cluster colors [SM Fig. 3 (f,g)] shows that CDW-1 and CDW-2 are arranged in the same 3D pattern as that of the pristine sample [Main Fig. 2 (b,c)]. The blue and red clusters identify with the primary CDW-1 and CDW-2 peaks, respectively, while the purple cluster captures the higher-order peaks of CDW-1. Having identified which pixel correspond to the CDW peaks, we can look at the average intensity of each cluster (the peak height of CDWs) [SM Fig. 3 (h)]. Compared to the pristine sample [Main Fig. 2 (a)], a 2% intercalation strongly suppresses the CDW-2 with no sharp onset behavior.

Filtering the CDW-1 peaks

In the previous section, we showed a brute-force XTEC analysis on the full data. That analysis identified the CDW peaks and their 3D structure in the reciprocal space. We can now more precisely target the CDW-1 peaks by filtering out only the pixels of the primary CDW-1 peaks with a mask. We apply the mask shown in SM Fig 4(a,b) on the raw intensities before feeding to XTEC. We select the mask with sufficiently large windows to capture broad peaks such that the results are robust to the size of the mask. The filtered intensities are then fed into the XTEC pipeline, as described in the previous section. A clustering on these filtered intensities [SM Fig 4 (c)] eliminates the background as well as the noisy and weak CDW-1 peaks (purple and thistle clusters). This procedure gives us a collection of $\sim 3,000$ intense and well-defined CDW-1 peaks (blue cluster) that can be robustly analyzed to extract their peak height and spread. The results in main Fig. 2(d-f) and Fig. 3 follow this analysis.

G: CONVENTIONAL PEAK WIDTH ANALYSIS

The conventional approach of extracting the peak width would be to take one-dimensional line cuts through CDW peaks in the binned data and extract intensity and width parameters from fitting. Fitting domains must be chosen arbitrarily in relation to diffuse scattering and spurious crystallographic imperfections, making this approach difficult to apply to the entire dataset. Moreover, the necessity of determining the goodness of fit makes this approach impractical to scale. Applying this approach to an ad-hoc choice of peaks at $hkl = 4\ 2\ 3 \pm q_c$ in SM Fig. 5 for the 2% intercalation shows that the spurious signals make it difficult to find a uniform way to fit even a small number of peaks in these data, and even the best-fitted parameters will have low precision. It is also clear from SM Fig. 5 that it is impossible to extract any power law tails from fitting these peaks. Thus, relying on power law tails as a signature of Bragg glass is not feasible.

The challenge in estimating the subtle peak height asymmetry or the profile asymmetry of the CDW satellite peaks in intercalated samples is also clear from SM Fig. 5. The peak intensities from the Gaussian fit on two pairs of satellite

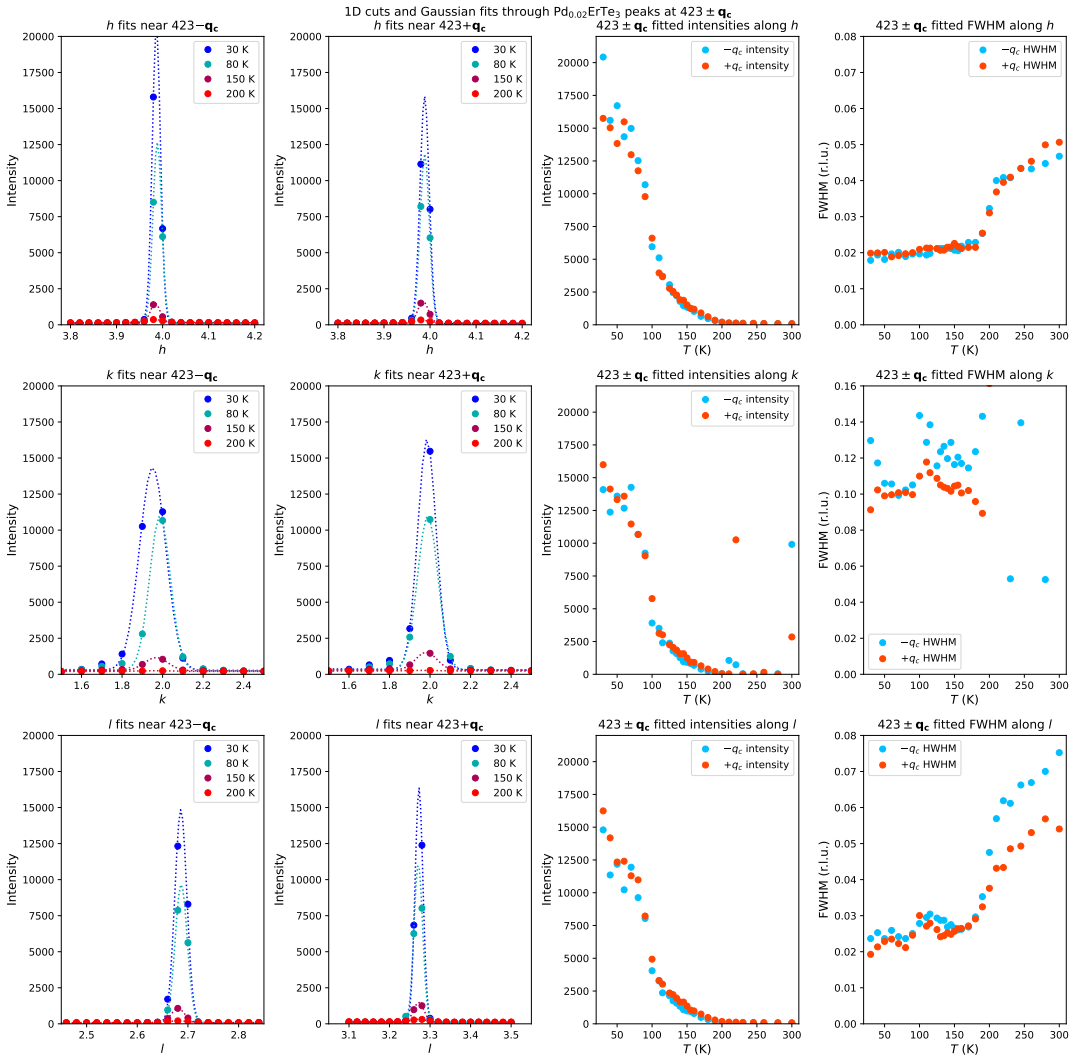

FIG. 5. A set of three one-dimensional Gaussian functions can be used to fit superstructure peaks and extract intensity and width parameters to characterize peaks. This approach is applied here to the $432 \pm \mathbf{q}_c, \mathbf{q}_c \approx \frac{2}{7}\mathbf{c}^*$ superstructure peaks in $Pd_{0.02}ErTe_3$. For all rows, the left two figures are cuts taken through superstructure peaks, with circles indicating data and dotted lines representing fitted Gaussians; the right two figures are fitted parameters at different temperatures. **Top row**: Line cuts taken along h. **Middle row**: Line cuts taken along k. Note that the peak become so broad along k above $T \approx 210$ K that the fitting function fails. **Bottom row**: Line cuts taken along l. It is notable that the full-width half maximum (FWHM) of the fit approaches the bin width at low temperatures, indicating that the peak is resolution-limited.

CDW-1 peaks do not reveal a stark asymmetry. Comparing the magnitude of the peak intensity (∼20,000 counts) and the strength of the asymmetry seen in the diffuse scattering (∼10 counts, see main Fig 4), the scale of asymmetry is too small to be detected from the fluctuations of peak height intensity. The peak widths of the two satellite peaks are also nearly identical, and hence we do not detect a clear signature of profile asymmetry.

H: EXTRACTING PEAK SPREAD ANALYSIS WITH *X-TEC*

In this section, we first provide details of the steps to extract the peak spread $\Gamma_{\vec{q}}(T)$ [Eq. (1) of main text] from the XRD data and benchmark them with line cuts on selected CDW-1 peaks [SM Fig. 6]. We then show the underlying quadratic momentum dependence of $\Gamma_{\vec{q}}$, and the extraction of the $\vec{q}$ independent term Γ_0 that quantifies the broadening purely due to CDW phase fluctuations [SM Fig. 8].

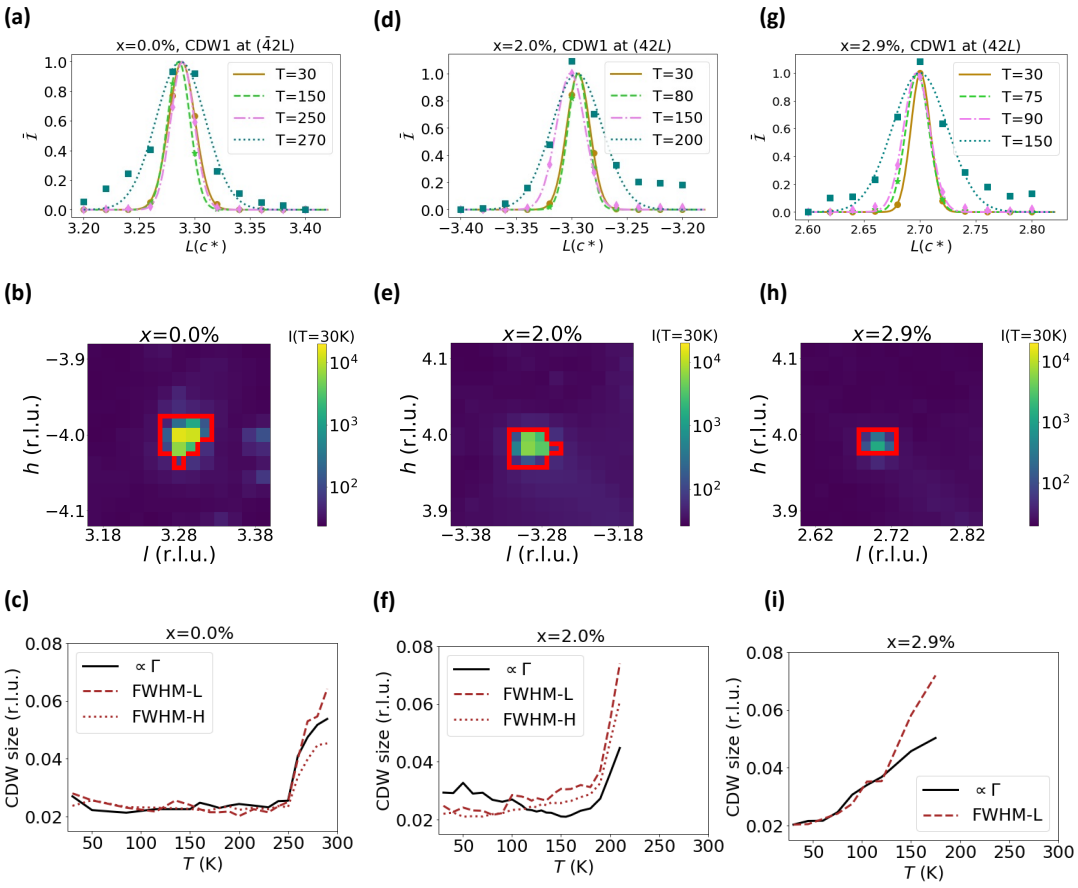

FIG. 6. Benchmarking the peak spread. **(a):** Line cut along a CDW-1 peak at various temperatures T for the pristine sample ($x = 0\%$). The intensities (symbols) are averaged along $H = \bar{4} \pm 0.02$ r.l.u and $K = 2$, and normalized with its maximum value at the peak. The minimum intensity in the line cut is subtracted to remove any background offset. The lines are Gaussian fits. **(b):** The intensity of the CDW-1 peak in the $K = 2$ plane [same peak as in (a)] at $T = 30$K, with the *X-TEC* determined peak boundaries (red contour) for the $x = 0\%$. **(c):** The peak spread (Γ) [Eq. (1) of main text] for the CDW peak in (a-b), along with the FWHM from line cuts along H (FWHM-H) and L (FWHM-L), at various T for $x = 0\%$. **(d,e,f):** Same as panels (a-c) respectively but for $x = 2\%$ intercalated sample. **(g,h,i):** Same as panels (a-c) but for $x = 2.9\%$ intercalated sample.

1. Benchmarking peak spread

The conventional approach to extract a FWHM is shown for a CDW-1 peak at the three levels of intercalation in SM Fig. 6 (a), (d) and (g). Our high throughput measure $\Gamma_{\vec{q}}$ [Eq. (1) of main text] directly provides a measure for the spread of the peak (in units of the number of pixels). This is achieved by using *X-TEC* to identify the connected pixels whose intensity trajectories belong to the CDW order parameter cluster. This is shown in SM Fig. 6 (b), (e) and (h), where the red boundary determined by *X-TEC* marks the extent of the CDW peaks. We quantify the spread of this CDW peak (centered at momentum $\vec{q}$) with $\Gamma_{\vec{q}}$ which is the ratio of the total intensity inside the peak boundary to the maximum intensity of the peak. We restrict to the in-plane peak spread with intensities at integer K values of the out of plane (b^*) axis, to avoid the lower resolution along b^* axis [0.1 (r.l.u.) compared to 0.02 (r.l.u.) for the in-plane] from limiting the overall resolution of the spread. The estimated $\Gamma_{\vec{q}}$ is compared with the FWHMs of the line cuts in SM Fig. 6 (c), (g) and (i). We see that the $\Gamma_{\vec{q}}$ faithfully captures the features of the FWHMs, in particular, the rapid onset of broadening above a transition temperature.

However, both the FWHMs and the $\Gamma_{\vec{q}}$ show an erratic temperature trajectory, reflecting the errors in the width estimation from the small resolution peaks (the peaks are roughly spread over 2-3 pixels). Collecting all $\Gamma_{\vec{q}}$ with $\vec{q}$ spanning ~ 3000 peaks, we find a wide variation in the range of values for the spread, [see SM Fig. 7 (a), (c), (e) and (g)]. Buried under these seemingly erratic trajectories is the systematic $\vec{q}$ dependence from lattice distortions [see SM Fig. 8] and the unique $\vec{q}$ independent spread Γ_0 of the disordered CDW [see Fig. 3 of main text].

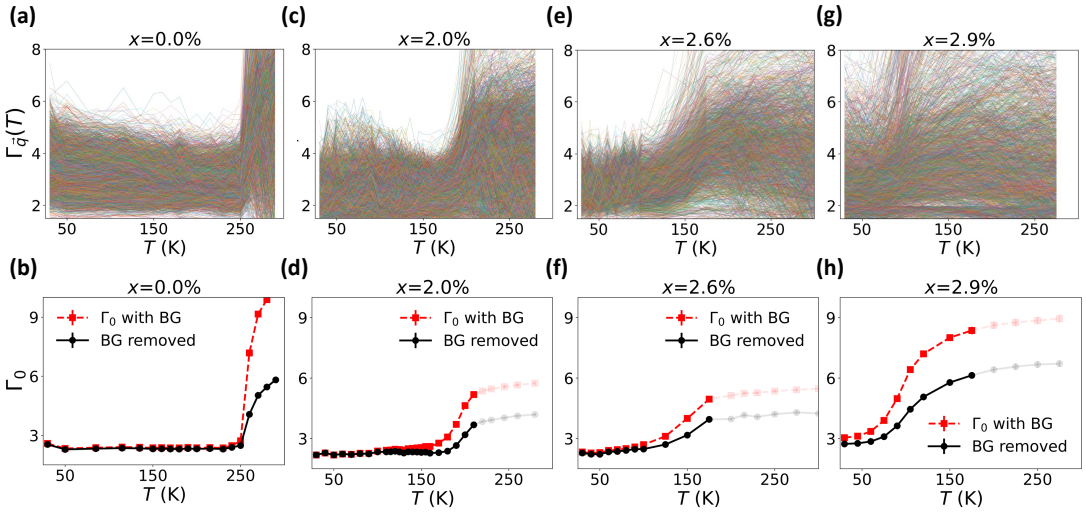

FIG. 7. Extracting the peak spread. **(a):** The T trajectory of the peak spread ($\Gamma_{\vec{q}}$) of 4877 CDW-1 peaks in the $x = 0\%$ data (thin colored lines). **(b):** Comparing Γ_0 with the background intensity offset removed (BG removed), and Γ_0 keeping the background offset (Γ_0 with BG). Lines are guides to the eyes. **(c,d):** Same as (a,b) respectively but for $x = 2\%$ sample with 3688 peaks. The peak spread saturates above a cutoff temperature. **(e,f):** $x = 2.6\%$ intercalated sample with 2251 peaks. **(g,h):** $x = 2.9\%$ with 2713 peaks. In panels (d), (f) and (h), the peak spread saturates above a cutoff temperature, when the peak intensity drops near the background value.

An important step in the estimation of $\Gamma_{\vec{q}}$ is the removal of the background intensity offset from the CDW peak intensities. This background contribution is estimated as the average of the intensities outside the CDW boundary in a 10x10 pixel neighborhood of the peak [the blue region outside the red boundary in SM Fig. 7 (b), (d), (f) and (h)], and this offset contribution is subtracted from the total and maximum intensity of the CDW peak before estimating Γ_q. In SM Fig. 7 (b), (d), (f) and (h), we show the effect of not removing the background offset on the Γ_0. Keeping the background intensity results in an overestimation of the spread, especially at higher temperatures where the peak height is smaller. This is because the peak spread measure misinterprets the extra background intensity outside the true peak as a genuine broadening of the peak.

In SM Fig. 7 (d), (f) and (h), the peak spread saturates at high temperatures above a cut-off temperature. Above this temperature, the peak spreads beyond the boundaries of the peak determined by *X-TEC* [SM Fig. 6 (b), (e), (h)]. This is also the point where the peak intensity drops low enough to a value near the background intensity (see Fig. 2(d) of main text).

2. Momentum dependence of peak spread

In SM Fig. 8, we show that the spread $\Gamma_{\vec{q}}$ in the XRD data has a systematic broadening with quadratic dependence in $\vec{q}$ as predicted in SM-E. To simplify the visualization of the 3D quadratic fit in Eq. (2) of main text, we project the momentum dependence of $\Gamma_{\vec{q}}$ to one direction by averaging over the other directions. We show the H^2 dependence of $\Gamma_{\vec{q}}$ in SM Fig. 8 (a), and the L^2 dependence in (c) and (e), for the three levels of intercalation. The $\Gamma_{\vec{q}}$ fits well with the quadratic function.

The full 3D fit of $\Gamma_{\vec{q}}$ using Eq. (2) of main text extracts the quadratic coefficients γ_H, γ_K, γ_L as well as the momentum-independent intercept Γ_0. While Γ_0 is reported in the main text [Fig. 3 (c-f)], in SM Fig. 8 (b), (d) and (f) we report their respective γ_H, γ_K, and γ_L values.

I: BRAGG GLASS IN $x = 0.5\%$ INTERCALATION.

We show the analysis of 0.5% sample separate from the main figures, as this sample showed a much larger mosaic spread compared to all other samples. In SM Fig. 9, we show the filtered CDW-1 peaks of the 0.5% intercalation.

Unlike the other intercalated samples (2%, 2.6%, and 2.9%), the 0.5% is much similar to the pristine sample, and

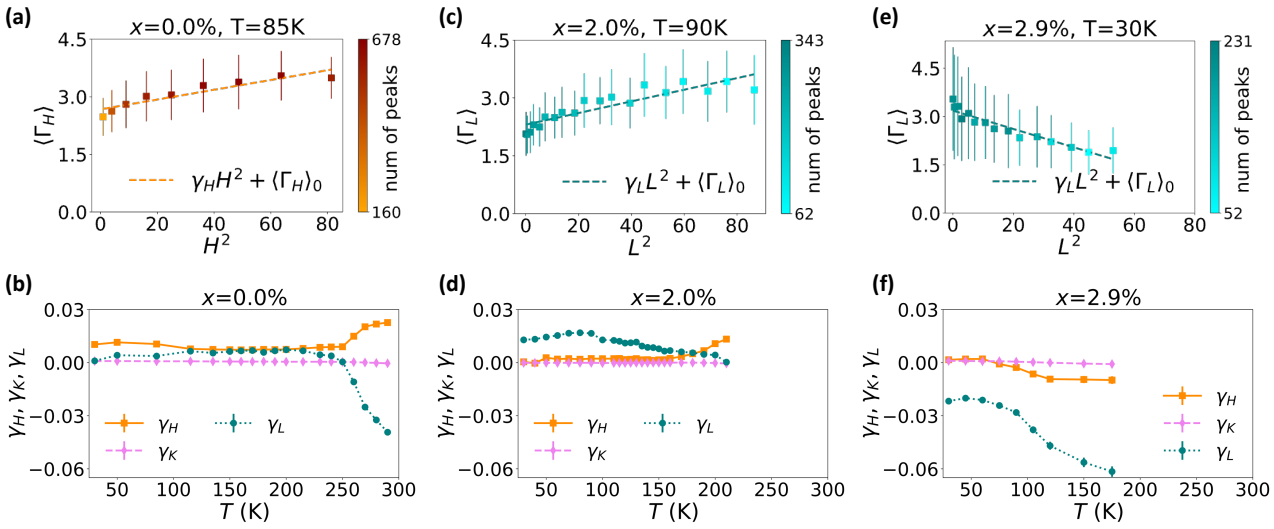

FIG. 8. **(a)**: The H^2 dependence of the peak spread in the $x = 0\%$ sample at T=85K. The $\langle\Gamma_H\rangle$ (symbols) is the spread obtained by averaging $\Gamma_{\vec{q}}$ over K and L that share the same $|H|$. The error bars indicate standard deviation of $\Gamma_{\vec{q}}$ at $|H|$. The markers are color-coded, and the color bar indicates the number of peaks determining the statistics of each marker. The fit: $\gamma_H H^2 + \Gamma_0$ agrees well with $\langle\Gamma_H\rangle$ within the error markers. **(b)**: The momentum coefficients γ_H, γ_K, γ_L from the 3D quadratic fit [Eq. (2) of main text] to $\{\Gamma_{\vec{q}}\}$ at various temperatures for the $x = 0\%$. The lines are guides to the eye. **(c)**: Same as (a) but for the L^2 dependence of the spread, $\langle\Gamma_L\rangle$ (symbols) (by averaging $\Gamma_{\vec{q}}$ over H and K at $|L|$) for the $x = 2\%$ intercalated sample at T=90K. The fit $\gamma_L L^2 + \langle\Gamma_L\rangle_0$ also agrees well within the standard deviation of $\Gamma_{\vec{q}}$ at L. **(d)**: Same as (b), but for the $x = 2\%$ intercalated sample. **(e-f)** Same as (c-d) respectively, but for $x = 2.9\%$ intercalated sample.

shows the BCS scaling order parameter Fig. 9(a), with a critical temperature of $235K$. The peak spread is shown in SM Fig. 9(b). Despite the similarity with the pristine sample, $x = 0.5\%$ is distinguished by the presence of asymmetry in the diffuse scattering [SM Fig. 9(c,d)]. The presence of the distinct half-diamond asymmetry, similar to that of other intercalated samples, shows that the 0.5% intercalation is disordered and different from the pristine sample. Thus, long range order is forbidden in this sample, and the transition temperature at $235K$ corresponds to a Bragg glass transition.

J: CDW SATELLITE PEAK ASYMMETRY.

In Fig 4 of the main text, we discussed the asymmetry in the diffuse scattering surrounding the CDW peaks. The diffuse scattering asymmetry is present only in intercalated samples, and clearly distinguishes them as disordered. In this section and in SM Fig 10, we investigate the asymmetry in the CDW peaks after removing the diffuse background. As will be apparent from the following discussion, this analysis is prone to errors from the pixelation of peaks and the interpolation of background diffuse scattering. Hence these results should be interpreted with a grain of salt.

We implement a punch-and-fill method to isolate the CDW peak heights from the diffuse background. As shown in SM Fig. 10 (a), we identify the pixels of the CDW peaks (enclosed within the red boundary) with *X-TEC*. These CDW pixels are punched out and filled with a linear spline interpolation of their neighboring intensities. A line cut through the CDW-1 satellite peaks shows the CDW peaks (solid lines) and the interpolated background (dashed line) in SM Fig. 10 (b). Subtracting the two isolates the CDW peaks from the diffuse scattering.

The background removed in-plane intensities of CDW-1 satellite peaks around the Bragg peak at $(H, L) = (1, 4)$ and K averaged along all values in $[-20, 20]$ is shown in SM Fig. 10 (c). Unlike the stark asymmetry apparent in the background, the asymmetry is not obvious in the CDW peaks and is subtle, if any, even for the strongest intercalation. Moreover, with only two data points to span the peaks, it is impossible to fit the peak profile.

Using the peak maxima as the estimate for the peak height, the asymmetry for the peaks around $(H, L) = (1, 4)$ is quantified in SM Fig. 10 (d), as $\alpha = (I_L - I_R)/(I_L + I_R)$ where I_L and I_R is the peak maxima of the left and right CDW peak. A noticeable asymmetry is seen for the 2.9% intercalation. However, the very small height of peaks of 2.9% (an order of magnitude smaller than the pristine and 2% intercalation) makes them more sensitive to errors in subtracting the background.

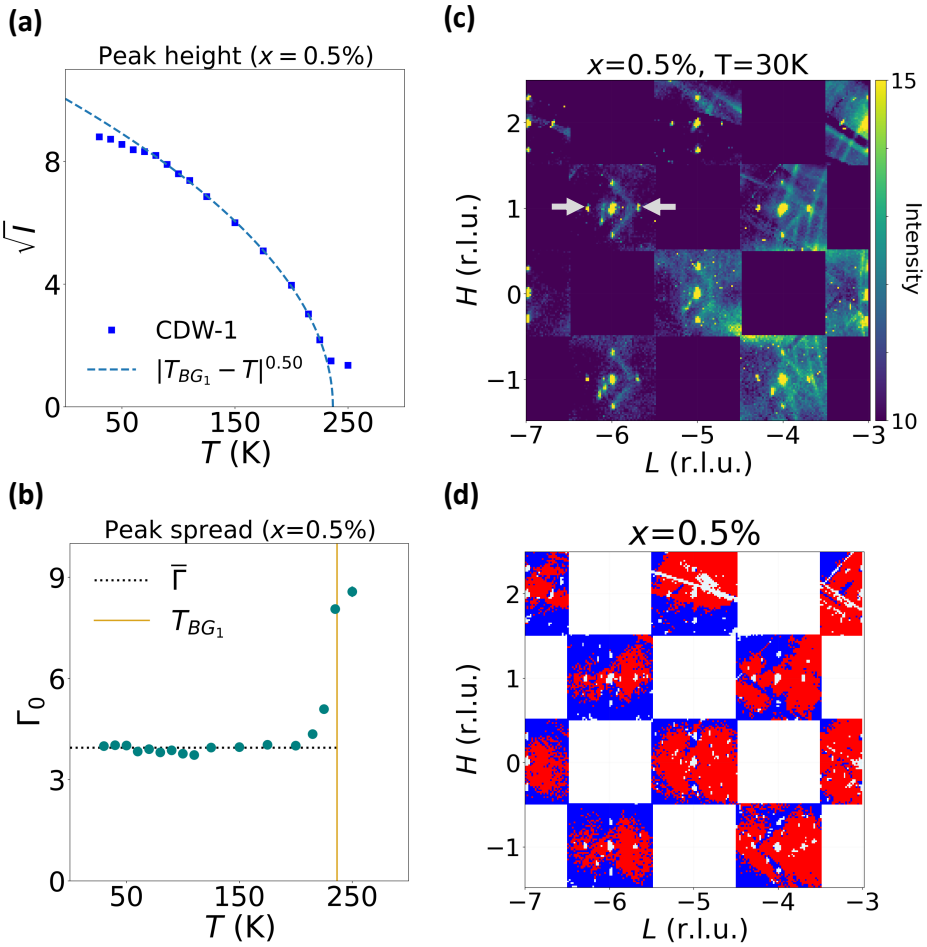

FIG. 9. x=0.5% sample. **(a):** The CDW-1 peak averaged intensity (peak height). The $\tilde{I}$ is obtained from the average of all the intensities in the CDW-1 cluster (2323 peaks), from which we subtract the background intensity contribution. $\sqrt{\tilde{I}(T)}$ fits well to a power law $\propto (T_{BG_1} - T)^{\beta}$ giving $T_{BG_1} \sim 235$K and $\beta = 0.5$ matching the BCS order parameter exponent. **(b):** The $\vec{q}$ independent broadening of CDW-1 peak spread, $\Gamma_0(T)$, extracted from 2323 peaks by fitting their $\Gamma_{\vec{q}}$ to a quadratic function of $\vec{q}$ [Eq. 2 of main text]. The $T_{BG_1} = 235$K extracted from panel (a) is also shown. **(c):** The intensity at $T = 30$K, in the H-L plane with $K = 1.0$, shows a diffuse scattering that is asymmetrically distributed between the two satellite peaks, in the form of half diamonds. (see arrows for reference) **(d):** Two cluster X-TEC results color coded as red and blue, from the temperature trajectories of the diffuse scattering intensities. The pixels are colored red (blue) if their intensity trajectory belongs to the red (blue) cluster. The intensities of the CDW peaks and H+L = odd Bragg peaks (white pixels, identified from a prior X-TEC analysis) are excluded from this two-cluster X-TEC, along with the H+L = even Bragg peaks removed by a square mask (square white regions)

For a more accurate and comprehensive estimate of the asymmetry ratio, in Fig. 10 (e), we measure the peak heights in the 2D (H, L) plane rather than along line-cuts. The panel shows the mean and standard deviation of asymmetry from all pairs of in-plane CDW satellite peak intensities in the $-1.5 \leq H \leq 2.5$ and $3 \leq L \leq 8.5$ (same region shown in Fig 4 (a-b) of main text). In this region, the asymmetry ratio of only those pairs of peaks that are present in all four samples are chosen. The figure suggests that intercalated samples have a slightly higher value of asymmetry than the pristine sample. However, the overall small values of the ratio and their large variance, as well as the susceptibility of the analysis to pixelation and background subtraction errors, prevent us from establishing conclusive evidence of asymmetry in the peak heights, even at the highest intercalation (x=2.9%) which is a clearly disordered sample. However, the diffuse asymmetry that surrounds the CDW peaks already makes the total peak height asymmetric [Fig. 4(c-e) of main text]. This is a clear sign that intercalation introduces disorder pinning to the modulations at and around the CDW.

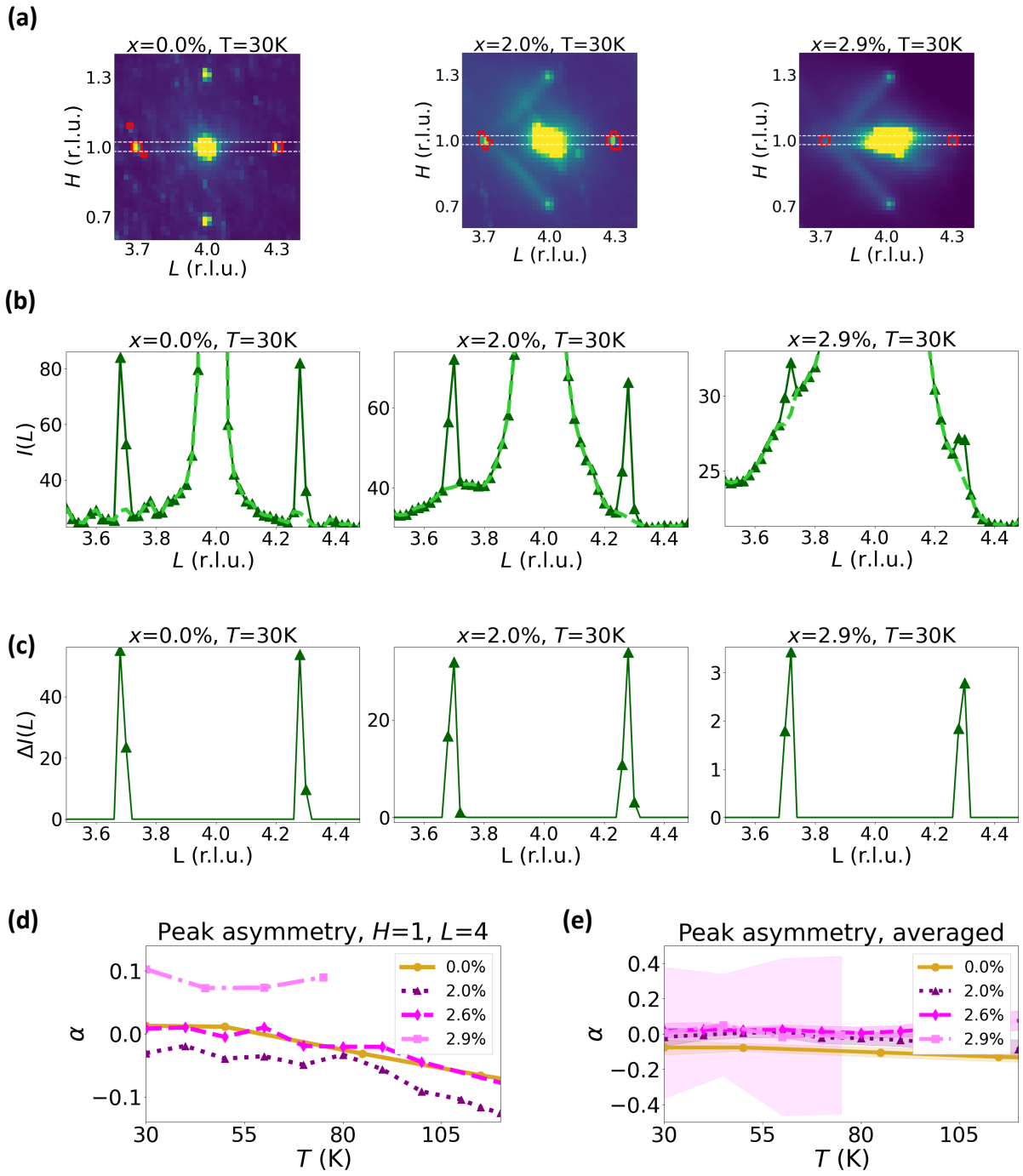

FIG. 10. CDW satellite peak asymmetry. **(a):** The in-plane XRD near the $(H = 1, L = 4)$ Bragg peak at $T = 30$K, with K (out-of-plane axis) averaged over all values between -20 and 20 (r.l.u). The pixels identified by X-TEC as CDW-1 peaks are enclosed within the red boundary. The horizontal dashed line marks the region considered for the line cuts in panel (b). **(b):** Line-cut intensities across the CDW-1 peaks along L with intensity averaged over $H \in [0.98, 1.02]$ (r.l.u) and $K \in [-20, 20]$ (r.l.u). The solid line shows the raw intensity, and the dashed line shows the interpolated intensities after removing the CDW pixels. **(c):** The CDW-1 peak intensities after subtracting the interpolated (dashed line) from the raw intensities (solid line) of the panel (b). **(d):** Asymmetry in the satellite peaks surrounding $(H = 1, L = 4)$, quantified by the ratio $\alpha = (I_L - I_R)/(I_L + I_R)$, where I_L and I_R are the heights of the left and right CDW-1 peak intensities. **(e):** Mean (lines) and standard deviation (shading) of α from all pairs of CDW satellite peaks in the $-1.5 \leq H \leq 2.5$ and $3 \leq L \leq 8.5$.

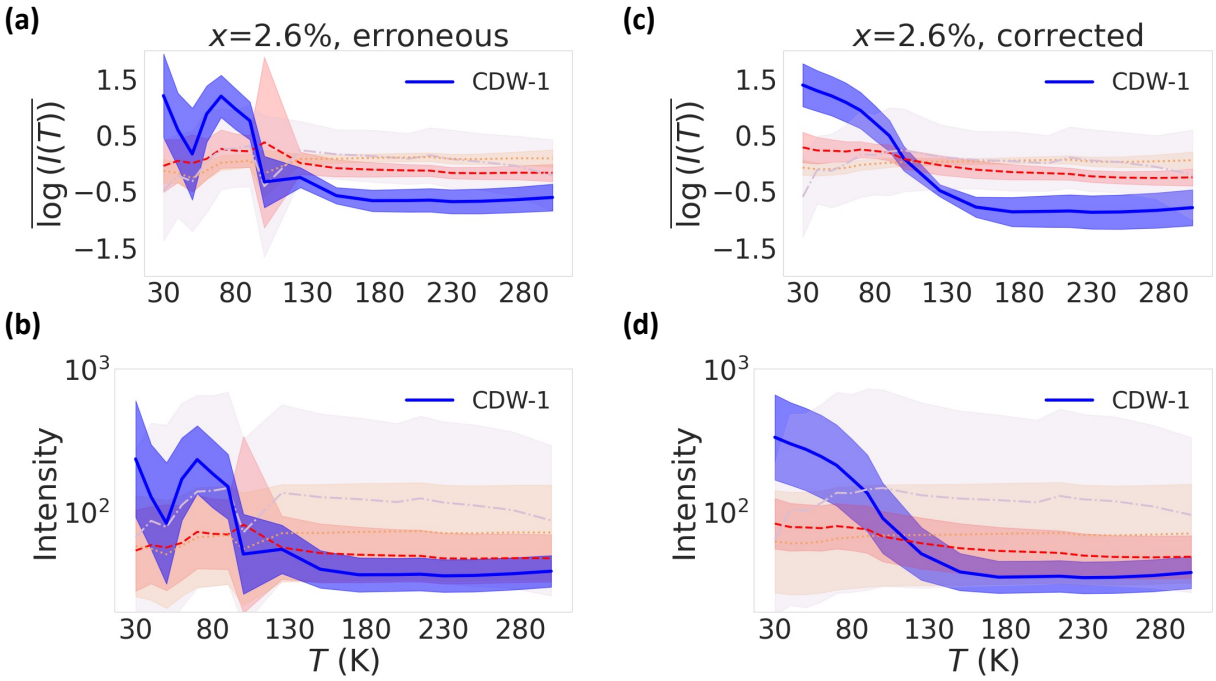

FIG. 11. **(a,b):** The *X-TEC* analysis on 2.6% intercalation, with a slight misorientation error during the image transformation to reciprocal space bins. The trajectory of all clusters including the blue CDW-1 cluster show sudden discontinuities. Panel (a) shows the cluster mean (lines) and variance (shading) of the GMM with rescaled intensities. Panel (b) shows the average and one standard deviation of the unscaled intensities in each cluster. **(c,d):** Same as panels (a) and (b) but for the correctly oriented transformation of the same 2.6% intercalation.

K: CAVEATS WITH THE IMPROPER ORIENTATION OF XRD TRANSFORMATION.

In this section, we discuss the importance of ensuring the correct orientation at each temperature during the transformation of images to the reciprocal space bins. In SM Fig:11, we show an instance of improper orientation on the 2.6% sample. In panels (a-b), we see the blue *X-TEC* cluster that identify with the CDW-1 have an anomalous hump, and an erratic trajectory. Sharp jumps in temperature are seen concurrently for all the clusters, including the CDW-1 cluster.

A more careful transformation of the same 2.6% data, where the reciprocal space images at different temperatures are ensured to have the same correct orientation, eliminates the erratic trajectories and sharp jumps. In SM Fig:11 (c,d), the *X-TEC* analysis shows smooth trajectories for the CDW-1 (blue cluster) as well as the other clusters of the diffuse background.

The *X-TEC* analysis thus makes it easy for the scientist to visually inspect orientation errors during the transformation of images to reciprocal space. A misorientation will show up as sharp discontinuities occurring concurrently in the majority of the clusters. These discontinuities should not be confused with a first-order phase transition, as in the latter; only the cluster that captures the order parameter shows the discontinuity, while the remaining clusters have smooth trajectories.

[1] Yoseph Imry and Shang-keng Ma, "Random-Field Instability of the Ordered State of Continuous Symmetry," Physical Review Letters **35**, 1399–1401 (1975).

[2] H. Fukuyama and P. A. Lee, "Dynamics of the charge-density wave. I. Impurity pinning in a single chain," Physical Review B **17**, 535–541 (1978).

[3] Thomas Nattermann, "Scaling approach to pinning: Charge density waves and giant flux creep in superconductors," Phys. Rev. Lett. **64**, 2454–2457 (1990).

[4] Alberto Rosso and Thierry Giamarchi, "X-ray spectrum of a pinned charge density wave," Physical Review B **70**, 224204 (2004).

[5] Thierry Giamarchi and Pierre Le Doussal, "Elastic theory of flux lattices in the presence of weak disorder," Physical Review B **52**, 1242–1270 (1995).

[6] Michel J. P. Gingras and David A. Huse, "Topological defects in the random-field XY model and the pinned vortex lattice to vortex glass transition in type-II superconductors," Physical Review B **53**, 15193–15200 (1996).

[7] T. Giamarchi and P. Le Doussal, "Phase diagrams of flux lattices with disorder," Physical Review B **55**, 6577–6583 (1997).

[8] N. Ru and I. R. Fisher, "Thermodynamic and transport properties of YTe_3, $LaTe_3$, and $CeTe_3$," Physical Review B **73**, 033101 (2006).

[9] J. A. W. Straquadine, F. Weber, S. Rosenkranz, A. H. Said, and I. R. Fisher, "Suppression of charge density wave order by disorder in Pd-intercalated $ErTe_3$," Physical Review B **99**, 235138 (2019).

[10] Matthew J Krogstad, Stephan Rosenkranz, Justin M Wozniak, Guy Jennings, Jacob P C Ruff, John T Vaughey, and Raymond Osborn, English"Reciprocal Space Imaging of Ionic Correlations in Intercalation Compounds," Nature Materials **19**, 63–68 (2020), 1902.03318.

[11] S. Ravy, S. Rouzière, J.-P. Pouget, S. Brazovskii, J. Marcus, J.-F. Bérar, and E. Elkaim, "Disorder effects on the charge-density waves structure in V- and W-doped blue bronzes: Friedel oscillations and charge-density wave pinning," Physical Review B **74**, 174102 (2006).

[12] Alberto Rosso and Thierry Giamarchi, "X-ray diffraction of a disordered charge density wave," Physical Review B **68**, 140201 (2003).

[13] Thierry Giamarchi and Pierre Le Doussal, "Elastic theory of pinned flux lattices," Phys. Rev. Lett. **72**, 1530–1533 (1994).

[14] A. Guinier, *X-Ray Diffraction: In Crystals, Imperfect Crystals, and Amorphous Bodies* (Dover Publications, New York, 1994).

[15] S Ravy, JP Pouget, and R Comes, "Destructive interferences between diffuse scatterings due to disorder and displacive modulation (x-ray "white line" effect)," Journal de Physique I **2**, 1173–1190 (1992).

[16] S. Ravy and J. P. Pouget, "Structural studies of the CDW interaction with defects," Le Journal de Physique IV **03**, C2–C2–114 (1993).

[17] V. J. Emery and J. D. Axe, "One-dimensional fluctuations and the chain-ordering transformation in $hg_{3-\delta}Asf_6$," Phys. Rev. Lett. **40**, 1507–1511 (1978).

[18] I. U. Heilmann, J. D. Axe, J. M. Hastings, G. Shirane, A. J. Heeger, and A. G. MacDiarmid, "Neutron investigation of the dynamical properties of the mercury-chain compound $hg_{3-\delta}Asf_6$," Phys. Rev. B **20**, 751–762 (1979).

[19] Richard D. Spal, Cynthia E. Chen, Takeshi Egami, Paul J. Nigrey, and Alan J. Heeger, "X-ray scattering study of one-dimensional lattice dynamics inhg3δasf6," Physical Review B **21**, 3110–3118 (1980).

[20] H. Endres, J.P. Pouget, and R. Comes, "Diffuse x-ray scattering and order-disorder effects in the iodide chain compounds n,n-diethyl-n,n-dihydrophenazinium iodide, e2pi1.6, and n,n-diebenzyl-n,n-dihydrophenazinium iodide, b2pi1.6," Journal of Physics and Chemistry of Solids **43**, 739–748 (1982).

[21] Jordan Venderley, Krishnanand Mallayya, Michael Matty, Matthew Krogstad, Jacob Ruff, Geoff Pleiss, Varsha Kishore, David Mandrus, Daniel Phelan, Lekhanath Poudel, Andrew Gordon Wilson, Kilian Weinberger, Puspa Upreti, Michael Norman, Stephan Rosenkranz, Raymond Osborn, and Eun-Ah Kim, "Harnessing interpretable and unsupervised machine learning to address big data from modern X-ray diffraction," Proceedings of the National Academy of Sciences **119**, e2109665119 (2022).

[22] Christopher M Bishop and Nasser M Nasrabadi, *Pattern recognition and machine learning*, Vol. 4 (Springer, 2006).

[23] F. Pedregosa, G. Varoquaux, A. Gramfort, V. Michel, B. Thirion, O. Grisel, M. Blondel, P. Prettenhofer, R. Weiss, V. Dubourg, J. Vanderplas, A. Passos, D. Cournapeau, M. Brucher, M. Perrot, and E. Duchesnay, "Scikit-learn: Machine learning in Python," Journal of Machine Learning Research **12**, 2825–2830 (2011).